PERGAMON

International Journal of Heat and Mass Transfer 42 (1999) 3739–3756

International Journal of HEAT and MASS TRANSFER

www.elsevier.com/locate/ijhmt

Conduction trees with spacings at the tips

Majed Almogbel, Adrian Bejan*

Department of Mechanical Engineering and Materials Science, Duke University, Box 90300, Durham, NC 27708-0300, USA

Received 22 October 1998; received in revised form 2 February 1999

Abstract

This paper documents two methods of improving the performance of volume-to-point tree networks for two-dimensional heat conduction. These improvements are offered relative to the design produced by the constructal method, in which optimized volume elements (building blocks) are presented and grouped into larger constructs, which are also optimized. The first improvement is that each construct is optimized with respect to all its degrees of freedom: unlike in the constructal method, the optimized features of the smaller building blocks are not preserved during the optimization of the construct. The second improvement opportunity is that spacings are allowed between the facing tips of neighboring high-conductivity inserts. All such spacings are optimized. Another new direction pursued in this paper is the optimization of tree networks that must fill a volume with prescribed external shape (e.g., square, or disk). The designs optimized numerically in this paper lower the volume-to-point resistance beyond the levels achieved based on the constructal method, and bring the shape of the conduction tree closer to the shapes seen in nature.

1. Constructal tree networks

A recent paper [1] described the problem of connecting with minimum thermal resistance a finite-size volume and a point-size heat sink. The volume generates heat at every point and has a relatively low thermal conductivity, k_0. Conduction is aided by distributing a finite amount of high conductivity material (k_p) through the heat generating volume. It was shown that the solution to this problem—the path of least global resistance—can be pursued in a sequence of optimization and construction steps, which starts from the smallest volume element and continues toward larger volumes (assemblies, constructs). Optimized at every step is the *geometry* of the system. The volume-to-point heat flow problem adds itself to a larger class of geometric optimization problems that have been identified and solved recently in the active field of electronics cooling (e.g., Refs. [2–6]).

A characteristic feature of each optimized building block is the *balance* between conduction (or temperature drop) through the k_0 medium and the k_p inserts. The visual manifestation of this balance is the optimal shape of each building block. As the building blocks coalesce into larger and larger assemblies, their high-conductivity inserts reveal the shape of a tree with thicker links near the root (heat sink). Every geometric feature of this shape is the result of the same generating principle: the minimization of volume-to-point resistance subject to volume and material constraints. Since this shape is deterministic (not random), and since it is constructed 'from small to large', the optimization principle was named *constructal*. The implications of this principle are great in physics and biology, because volume-to-point flows dominate most inanimate and animate flow systems in nature. Some of these applications are reviewed in Ref. [7].

* Corresponding author. Tel.: +1-919-660-5310; fax: +1-919-660-8963.

E-mail address: abejan@acpub.duke.edu (A. Bejan)

0017-9310/99/$ - see front matter
PII: S0017-9310(99)00051-4

Nomenclature

A	area [m^2]
A_p	area covered by k_p material [m^2]
B	length of k_p blade [m]
D	thickness of k_p blade [m]
H	height of conducting domain [m]
k_p	high thermal conductivity [W/m K]
k_0	low thermal conductivity [W/m K]
$\tilde{k}$	conductivity ratio (k_μ/k_0)
L	length of conducting domain [m]
n_1	number of elements in the first construct
n_2	number of first constructs in the second construct
q'''	volumetric heat generation rate [W/m^3]
S	tip spacing [m]
T	temperature [K]
x, y	Cartesian coordinates [m]

Greek symbol

ϕ	volume fraction of k_p material

Subscripts

m	minimized once
min	minimum
opt	optimum
peak	peak temperature, hot spot
th	theoretical
0	elemental volume
1	first construct, assembly
2	second construct, assembly

Superscript

$\sim$	dimensionless notation, Eqs. (3)

The work reported in the present paper improves the constructal method in two significant ways. First, in the original formulation of the volume-to-point problem [1] it was assumed that the optimal shapes determined for one volume size (building block) are preserved and used at the next level of assembly, where a larger volume is covered with the optimized building blocks. This assumption simplified the optimization of the assembly by reducing its number of geometric degrees of freedom. No such assumption is made in the present work: each volume size is optimized with respect to all its degrees of freedom, regardless of the complexity of the internal structure that develops. We show that by giving the design more degrees of freedom we can raise its performance to levels higher than in Ref. [1].

The second improvement follows from allowing the tip of each high-conductivity insert to be surrounded by heat generating material. In the first demonstration of the constructal principle [1] it was assumed, for simplicity, that each high-conductivity insert stretched all the way across the volume element. When the elements were assembled into constructs, the adiabatic tips of the elemental inserts touched, and the resulting tree network had the appearance of a grid. In the present work this simplifying assumption is abandoned. By allowing spacings between the tips, and by optimizing these spacings we bring the performance of the conduction tree to higher levels. We also bring the image of the optimized tree closer to the shape seen in natural flow patterns.

2. Numerical formulation

Consider the two-dimensional conduction domain shown in Fig. 1. The total area is fixed ($H_0L_0 = A_0$), but the shape H_0/L_0 may vary. The domain contains

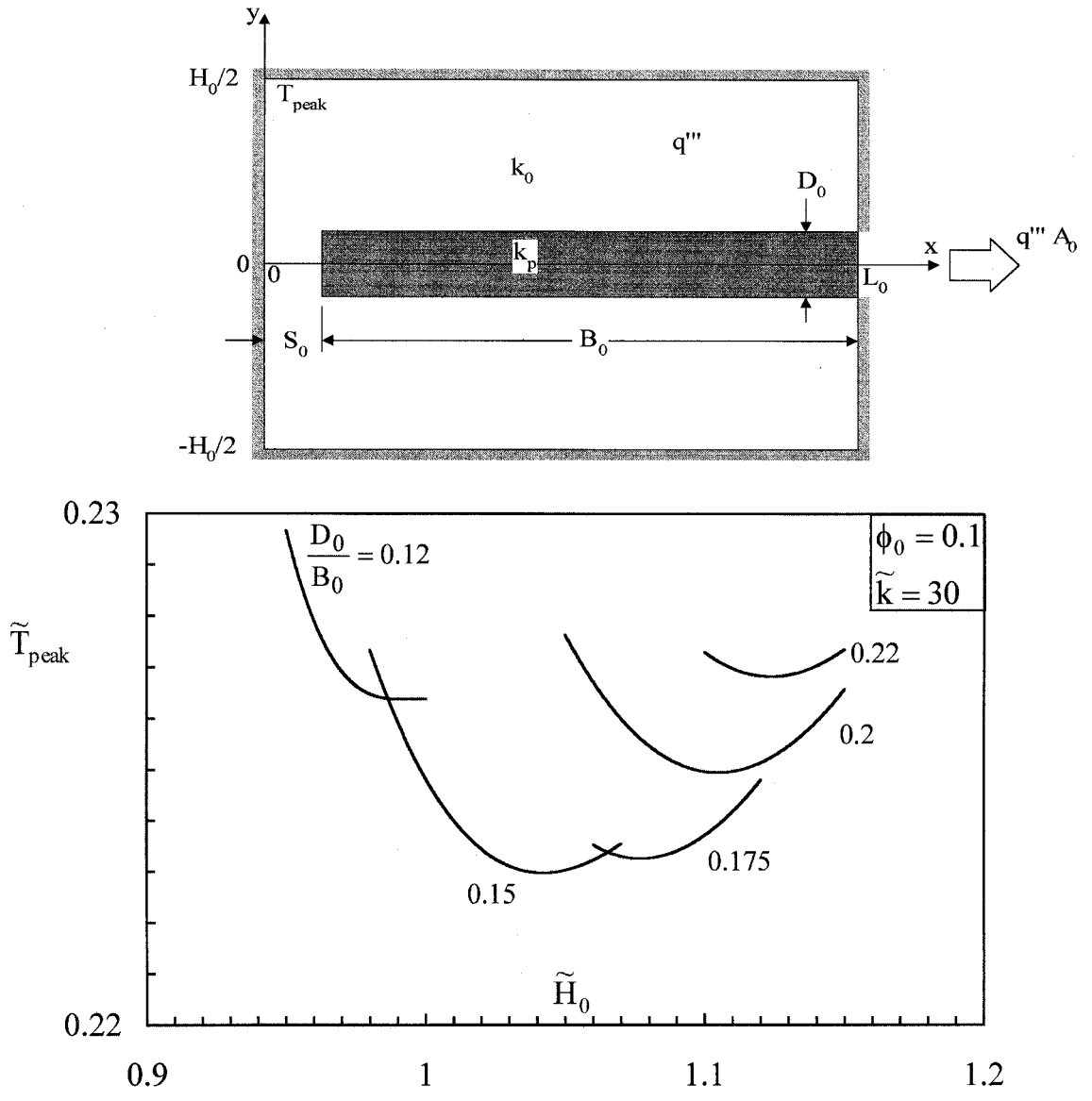

Fig. 1. Elemental conduction system with spacing at the tip of the high-conductivity insert, and the double minimization of its peak temperature.

two conducting materials. The low-conductivity material (k_0) fills most of the space and generates heat uniformly at every point (q‴). The high-conductivity material (k_p) is inserted as a blade of thickness D_0 and length B_0. The purpose of this blade is to collect the generated heat current, and to lead it out of the volume through a patch (heat sink) located at $x=L_0$ and $y=0$. The rest of the perimeter of the $H_0 \times L_0$ rectangle is insulated.

The high-conductivity blade does not penetrate all the way across the heat generating domain. There is a spacing ($S_0=L_0-B_0$) between its tip and the insulated side of the domain. This spacing may vary. Constrained is the amount of high-conductivity material ($A_{p0}=D_0B_0$), which can be expressed as a fraction of the overall size of the domain,

$$\phi_0 = \frac{A_{p0}}{A_0} = \frac{D_0 B_0}{H_0 L_0} \text{ (constant)} \tag{1}$$

In the steady state, the domain develops a temperature field that drives the generated current (q‴A_0, constant)

toward the point (L_0, 0). The highest temperature (T_{peak}) is recorded in the two corners (0, $\pm H_0/2$) that are situated the farthest from the heat sink. The objective of the numerical work was to minimize the highest temperature through changes in the architecture of the conducting system. This is equivalent to minimizing the overall thermal resistance between the finite-size volume and the point-size heat sink. There are two geometric parameters (two degrees of freedom) in this configuration, namely, the overall shape (H_0/L_0), and the shape of the high-conductivity profile (D_0/B_0). The second degree of freedom can also be represented by the tip spacing, for example, the ratio S_0:H_0.

The equation for steady state conduction through the k_0 material is

$$\frac{\partial^2 \tilde{T}}{\partial \tilde{x}^2} + \frac{\partial^2 \tilde{T}}{\partial \tilde{y}^2} + \frac{1}{1-\phi_0} = 0 \tag{2}$$

where the dimensionless variables are defined by

$$(\tilde{x}, \tilde{y}) = \frac{(x,y)}{A_0^{1/2}} \quad \tilde{T} = \frac{T - T(L_0,0)}{q''' A_0/k_0} \tag{3}$$

The corresponding equation for steady state conduction in the k_p material is

$$\frac{\partial^2 \tilde{T}}{\partial \tilde{x}^2} + \frac{\partial^2 \tilde{T}}{\partial \tilde{y}^2} = 0 \tag{4}$$

In this formulation, the dimensions of the rectangular domain are $(\tilde{H}_0, \tilde{L}_0) = (H_0, L_0)/A_0^{1/2}$ such that the overall size constraint reads $\tilde{H}_0 \times \tilde{L}_0 = 1$. The continuity of heat flux across the interface between the k_0 and k_p materials,

$$\left(\frac{\partial \tilde{T}}{\partial \tilde{n}}\right)_{k_0} = \tilde{k}\left(\frac{\partial \tilde{T}}{\partial \tilde{n}}\right)_{k_p} \tag{5}$$

reveals a second dimensionless parameter

$$\tilde{k} = \frac{k_p}{k_0} \tag{6}$$

Parameters ϕ_0 and $\tilde{k}$ describe the internal composition of the heterogeneous material that fills the elemental volume. For example, the analytical solution reported in Ref. [1] corresponds to the combined limit $\tilde{k} \gg \phi_0^{-1} \gg 1$ in a configuration like Fig. 1 but without spacing at the tip of the k_p blade ($S_0 = 0$). Indeed, the objective of the numerical work summarized in the next section was to document the effect of finite ϕ_0 and $\tilde{k}$ values in the configuration with finite spacing S, and to evaluate the goodness of the finite-S design relative to the $S = 0$ design optimized in Ref. [1].

3. Optimal elemental geometry

The numerical work consisted of determining the temperature field $T(\tilde{x}, \tilde{y})$ in a large number of configurations of the type shown in Fig. 1. The external and internal shapes (H_0/L_0, D_0/B_0) were changed only slightly from one configuration to the next. The material parameters $\tilde{k}$ and ϕ_0 were held fixed during each geometric optimization sequence. The calculated peak temperature $\tilde{T}_{peak}$ emerged as a function of the two shape parameters.

It is a characteristic feature of the constructal method that the optimization work, even when conducted numerically, is not based on a black-box optimization routine. The reason is that the elemental configuration (Fig. 1) is simple enough that we already know (analytically in certain limits [1]) that it has only one extremum. This is also clear from Fig. 1.

The bigger point is that we are making a deliberate effort to perform the optimization explicitly, for one degree of freedom at a time, by involving only one optimization principle: the maximization of thermal conductance subject to constraints. We think that *the principle generates the architecture* of the flow system (internal structure, external shape) [7]. We think that this—the principle—is important with regard to natural flow systems, because it empowers us with determinism (theory) in understanding and predicting such images.

The alternative, tried in the recent past, is to use a black-box optimization code to vary randomly all the possible geometric features of the flow paths, and to retain the changes that push the global volume-point resistance lower (subject to fixed volume and external shape). This technique leads to tree-shaped paths—a different tree each time that the code is run, because the search is random. The multitude of such near-optimal solutions is why many extrema exist in the region of minimum global resistance. This technique, however, is nondeterministic, which is why the tree image has been waiting for a purely theoretical explanation, in the same way that the round cross-section of the bronchial tube or earthworm have been explained based on resistance minimization [7].

In the present work, Eqs. (2) and (4) were solved using a finite elements code (FE) [8]. The accuracy of the FE code was tested against a finite differences code (FD) based on the Cholesky back-substitution method developed by ourselves and used extensively [9]. The FE code was necessary for this geometric optimization problem because we needed a reliable and flexible solver capable of handling efficiently very large matrices. The grids were nonuniform in both x and y, and their fineness was tested from one geometric configuration to the next. The grid was selected such that the dimensionless temperature results were insensitive

Table 1
Comparison between the hot-spot temperature results calculated with the finite-elements and finite-differences codes ($\phi_0=0.1$, $H_0/L_0=1$, $D_0/B_0=0.15$)

$\tilde{k}$	FE	FD
1000	0.128236	0.128979
300	0.135924	0.135408
100	0.157219	0.152994
30	0.224812	0.218397
10	0.374893	0.375390

to further grid doubling in both directions. Specifically, the grid was refined up to 10^4 nodes in some cases, to ensure that the further doubling of the number of nodes resulted in changes of less than 0.05% in the hot-spot temperature. The average number of nodes for all the simulations was 6000. Quadrilateral elements with biquadratic interpolation functions were used. Table 1 shows the close agreement between the hot spot temperature ($\tilde{T}$ at $x=0$ and $y=H_0/2$) calculated with the FE code and the corresponding values determined with the FD code.

The lower part of Fig. 1 shows the optimization path followed in each case ($\tilde{k}$, ϕ_0). The peak temperature was first minimized with respect to the external shape, which is represented by the dimensionless height of the elemental domain, $\tilde{H}_0$ (note that $H_0/L_0=\tilde{H}_0^2$). In the second round, the shape of the k_p insert was optimized by locating the minimum of the envelope of the curves shown in Fig. 1. In the end, every geometric detail of the elemental configuration (including the tip spacing S_0) was a result of the geometric minimization of the overall resistance to volume-to-point heat flow.

Table 2 is a summary of the optimal geometries determined for five cases in the range $30 \le \tilde{k} \le 300$ and $0.01 \le \phi_0 \le 0.1$. The pictorial presentation of the same geometries is the object of Fig. 2. The external slenderness ratio $(H_0/L_0)_{opt}$ increases as ϕ_0 and $\tilde{k}$ decrease. The internal slenderness ratio $(D_0/B_0)_{opt}$ decreases as ϕ_0 decreases, and increases as $\tilde{k}$ decreases. The table also shows the twice minimized peak temperature, where $\tilde{T}_{mm} \equiv \tilde{T}_{peak,min,min}$.The corresponding theoretical results for the limit $\tilde{k} \gg \phi_0^{-1} \gg 1$ and $S_0=0$ are [1]

$$\left(\frac{H_0}{L_0}\right)_{opt,th} = 2(\tilde{k}\phi_0)^{-1/2} \tag{7}$$

$$\tilde{T}_{mm,th} = \frac{1}{2}(\tilde{k}\phi_0)^{-1/2} \tag{8}$$

Note that when the tip spacing S_0 is zero and ϕ_0 is fixed, there is only one degree of freedom in the geometric optimization of the elemental volume: the overall shape H_0/L_0. Table 2 shows a comparison between (i) the optimized shape and twice-minimized peak temperature of the finite-S_0 configuration of Fig. 1, and (ii) the optimized ratio $H_0{:}L_0$ and once-minimized peak temperature of the $S_0=0$ configuration of Ref. [1]. The ratios $(H_0{:}L_0)_{opt}{:}(H_0{:}L_0)_{opt,th}$ and $\tilde{T}_{mm}{:}\tilde{T}_{mm,th}$ deviate by no more than 23% from the value 1. This means that the asymptotic solution of Ref. [1] can be used as a rough estimate of the best design and performance that can be achieved by optimizing the configuration of Fig. 1, which is more complicated than the configuration of Ref. [1]. Eq. (7) can also be used as a starting point in the numerical search for the optimal shape parameters (H_0/L_0, D_0/B_0) of Fig. 1.

The other practical message of the ratio $\tilde{T}_{mm}{:}\tilde{T}_{mm,th}$ listed in Table 2 is the benefit that can be expected from using the finite-S_0 geometry of Fig. 1, relative to the $S_0=0$ geometry of Ref. [1]. The relative reduction in the minimized volume-to-point resistance (or $\tilde{T}_{mm}$) can be of order 20% or greater. The payoff is larger when the product $\tilde{k}\phi_0$ is smaller, i.e., in the ($\tilde{k}$, ϕ_0) range where the analytical solution [1] is not valid. In conclusion, the numerical optimization of the geometry becomes a necessity when the product $\tilde{k}\phi_0$ is of order 1 or smaller.

The approximate agreement between the numerical value $(H_0/L_0)_{opt}$ and the analytical result for $(H_0/L_0)_{opt,th}$, Eq. (7), shows us an interesting way to anticipate the numerical results for the internal optimal shape parameter, (D_0/B_0), or the optimal spacing S_0. We reason as follows. The tip of the k_p insert (Fig. 1) acts as heat sink for two heat generating areas of con-

Table 2
Numerical results for the optimized geometry of the elemental volume of Fig. 1

ϕ_0	$\tilde{k}$	$(\frac{H_0}{L_0})_{opt}$	$(\frac{D_0}{B_0})_{opt}$	$\tilde{T}_{mm}$	$\frac{(H_0/L_0)_{opt}}{(H_0/L_0)_{opt,th}}$	$\frac{\tilde{T}_{mm}}{\tilde{T}_{mm,th}}$	$2(\tilde{k}\phi_0)^{1/2}(S_0/H_0)_{opt}$
0.1	30	1.082	0.150	0.2230	0.94	0.77	0.48
0.1	100	0.664	0.074	0.1375	1.05	0.87	0.50
0.1	300	0.384	0.040	0.0838	1.05	0.92	0.56
0.03	300	0.624	0.020	0.1493	0.94	0.89	0.31
0.01	300	1.024	0.013	0.2364	0.89	0.82	0.37

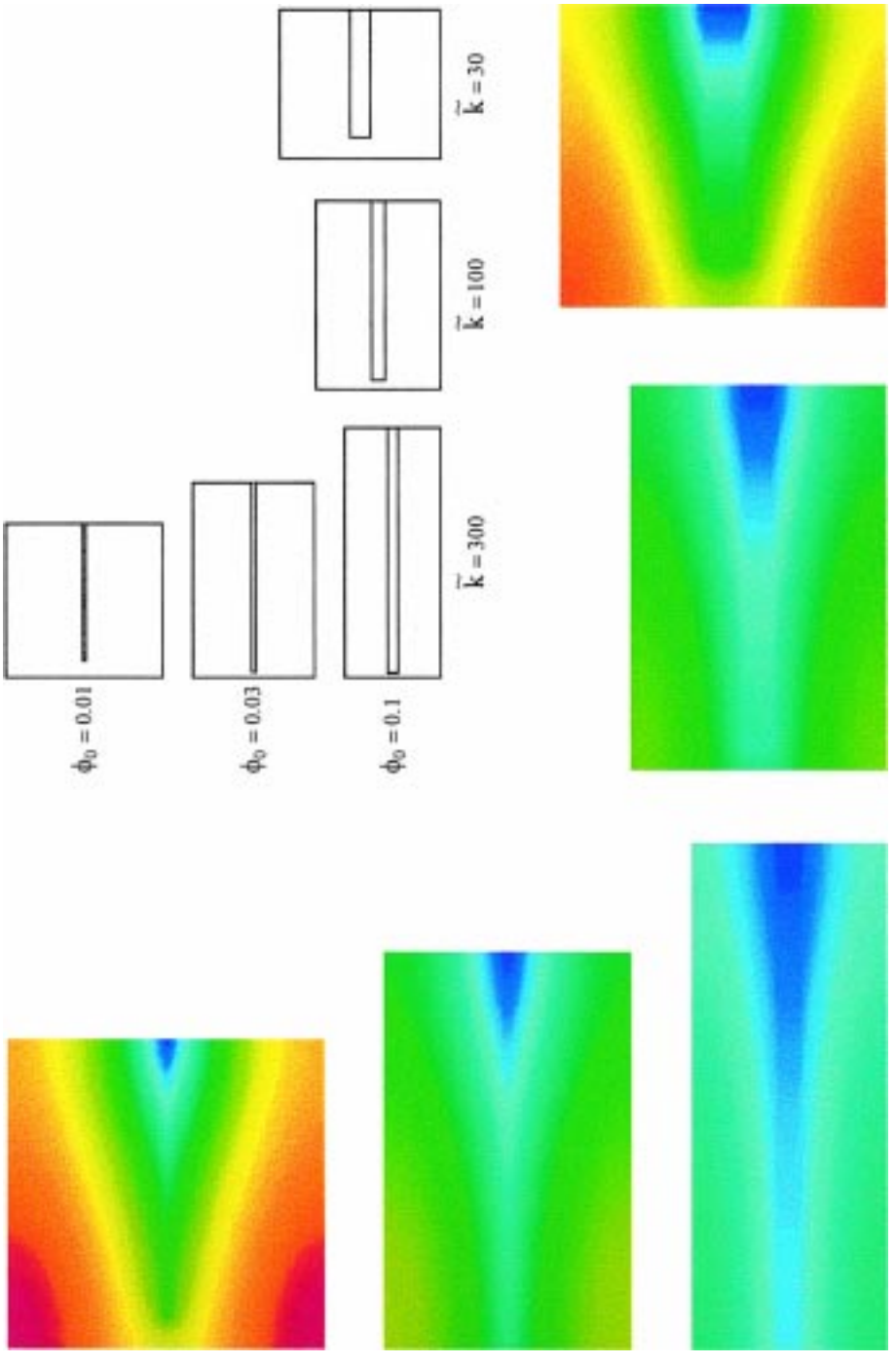

Fig. 2. The optimized geometry of the elemental conduction system, and the corresponding patterns of isotherms.

Table 3
The optimized internal geometry of an elemental volume shaped as a square

ϕ_0	$\tilde{k}$	$(D_0/B_0)_{opt}$	$\tilde{T}_m$	$2(\tilde{k}\phi_0)^{1/2}(S_0/H_0)_{opt}$
0.1	10	0.230	0.364	0.72
0.1	25	0.145	0.242	0.54
0.1	100	0.118	0.150	0.49
0.1	250	0.113	0.128	0.57
0.1	550	0.110	0.119	0.70
0.05	300	0.055	0.145	0.36
0.1	300	0.110	0.125	0.51
0.2	300	0.230	0.105	1.04
0.3	300	0.355	0.089	1.54

ductivity k_0 and size $S_0 \times (H_0/2)$, in the same sense that the root point (L_0, 0) acts as heat sink for two heat generating areas of conductivity k_0 and size $(H_0/2) \times L_0$. Consequently, we expect the following proportionality between the optimized aspect ratios of the respective k_0 domains,

$$2\left(\frac{S_0}{H_0}\right)_{opt} \sim \frac{1}{2}\left(\frac{H_0}{L_0}\right)_{opt,th} \quad (9)$$

which in view of Eq. (7) means that the group $(2\tilde{k}\phi_0)^{1/2}(S_0/H_0)_{opt}$ should be a number of order 1. The last column in Table 2 confirms the constancy of this order of magnitude, where the value of the calculated group is more closely approximated by 0.5.

4. Elemental system with fixed external shape

An important problem that was side-stepped entirely in Ref. [1] is the minimization of the volume-to-point flow resistance in situations where the shape of the given volume is fixed. In the fluid-flow illustration that is provided by the air passages of the human lung, the fixed shape of the total volume is the shape of the chest cavity. In the configuration of Fig. 1, the problem consists of determining only the optimal shape (or depth of penetration B_0) of the high-conductivity insert. The numerical optimization procedure is simpler than in sections 2 and 3, because this time there is only one degree of freedom: the ratio $D_0{:}B_0$, or the tip spacing ratio $S_0{:}H_0$.

Table 3 shows the optimal internal geometry of an elemental volume shaped as a square ($H_0/L_0 = 1$). The once-minimized peak temperature is indicated by $\tilde{T}_m = \tilde{T}_{peak,min}$. The slenderness ratio $(D_0{:}B_0)_{opt}$ decreases monotonically as $\tilde{k}$ increases and as ϕ_0 decreases. The optimal tip spacing continues to obey the order of magnitude expression derived based on Eq. (9).

A geometry related to that of Fig. 1 is the elemental volume with round cross-section which is cooled by a blade insert of length B_0 and thickness D_0 (Fig. 3, top). In this geometry the hot spot occurs at two points on the insulated circular perimeter, and moves as the shape of the internal blade changes. The internal aspect ratio $D_0{:}B_0$ can be optimized such that the hot-spot temperature is minimum. The results are shown in the lower part of Fig. 3. The trends and orders of magnitude are similar to those determined for the square volume with the same external dimension H_0. One peculiarity of the results for the circular cross-section are the minima exhibited by both $(D_0/B_0)_{opt}$ and $\tilde{T}_{peak,min}$ with respect to the conductivity ratio $\tilde{k}$.

5. Optimal first-assembly geometry

It was shown in Ref. [1] that additional reductions in global thermal resistance can be achieved in a sequence of steps in which the complexity of the high-conductivity paths increases, and where the geometric configuration is optimized at every step. The first step in this direction is shown in the upper part of Fig. 4. The high-conductivity inserts form a tree that may be viewed as an assembly of an even number of elemental volumes, $n_1 = A_1/A_0$. The overall size $A_1 = H_1L_1$ is fixed, and so is the volume fraction occupied by k_p material, $\phi_1 = A_{p1}/A_1$, where A_{p1} is the shaded area. The D_0 blades of the n_1 elements serve as tributaries to a central stem of thickness D_1. The tips of all the blades are surrounded by heat-generating k_0 material.

The first-assembly configuration has four degrees of freedom, which are represented by the dimensionless numbers n_1, H_1/L_1, D_1/D_0 and S_0/D_0. The S_1 spacing at the tip of the D_1-thick blade can be calculated later by noting that $H_0 = L_1/(n_1/2)$ and $S_1 = (H_0 - D_0)/2$. Similarly, the B_0 length of the D_0-thick blades follows from $L_0 = H_1/2$ and $B_0 = L_0 - S_0$. The combination of k_0 and k_p materials in each design is represented by the dimensionless parameters $\tilde{k}$ and ϕ_1, which were held fixed during each act of geometric optimization.

The numerical work was based on the same formalism as in section 2, except that ϕ_1, L_1 and A_1 replace ϕ_0, L_0 and A_0 in Eqs. (2) and (3). The optimization was performed with respect to the four degrees of freedom. The search for the optimum was organized in nested optimization loops—one loop for each degree of freedom. The peak dimensionless temperature exhibited minima with respect to H_1/L_1, D_1/D_0 and S_0/D_0, but not with respect to n_1. This feature distinguishes the present 'inward' design from the constructal approach described in Ref. [1]: when the aspect ratio H_0/L_0 optimized at the elemental level is carried over (preserved, memorized) at the first-assembly level, there is an optimal number of elements n_1. In general,

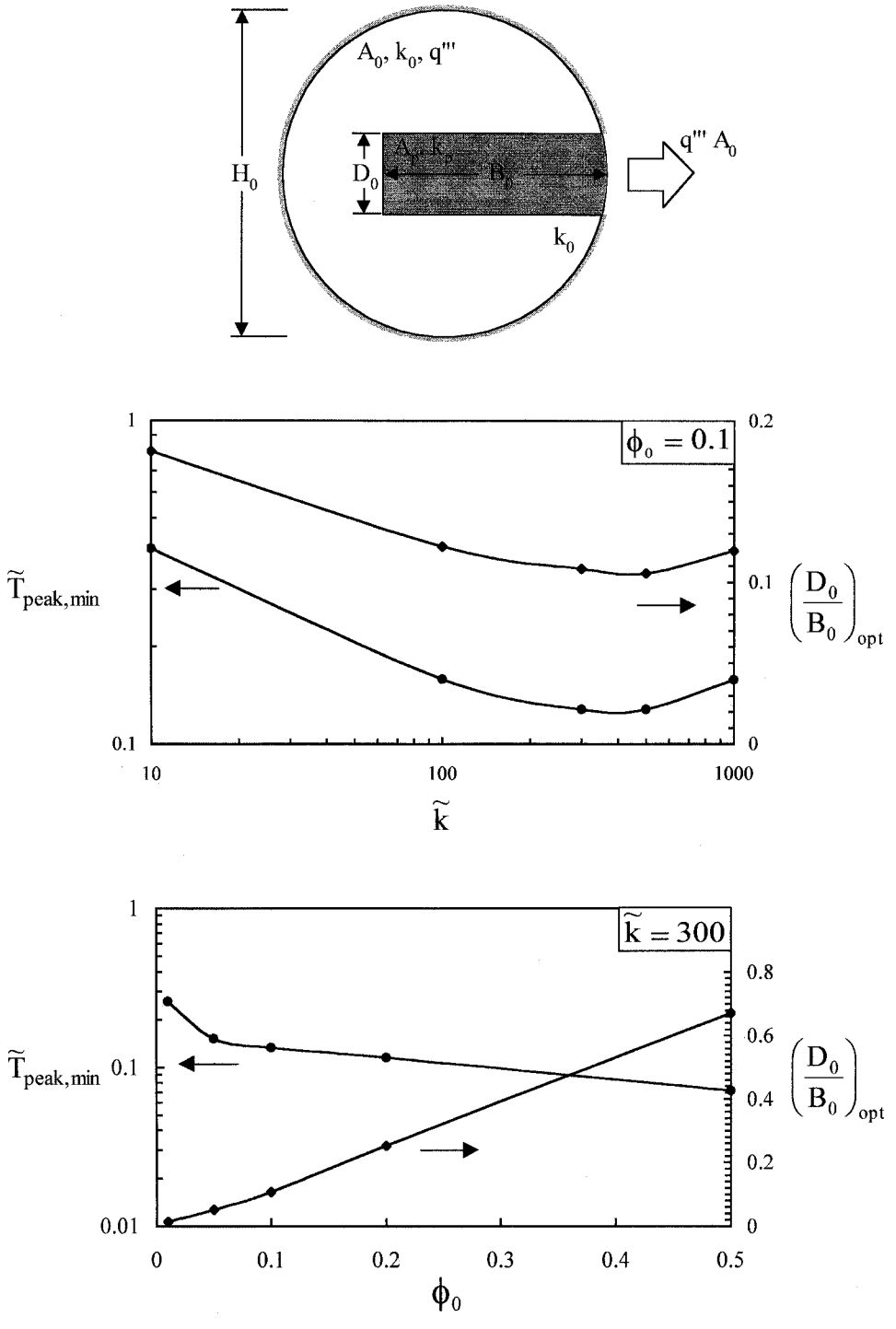

Fig. 3. The optimized internal geometry of an elemental volume shaped as a disk.

the optimized inward design should have an overall resistance that is lower than in the constructal case, because the inward optimization is less constrained. We discuss the relative merits of the two approaches in section 8.

The lower part of Fig. 4 is a scale drawing that

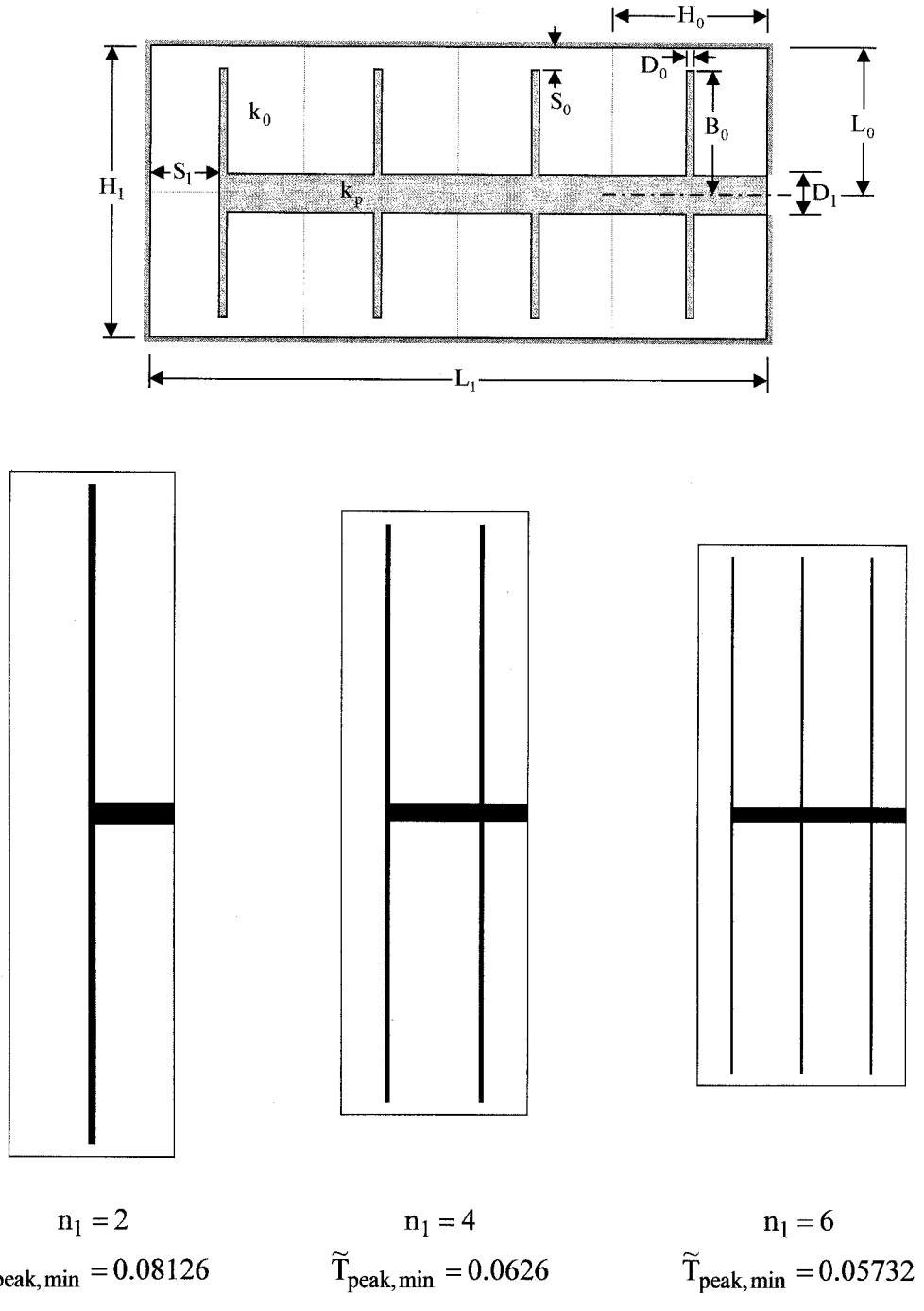

Fig. 4. First-assembly configuration with spacings at the tips of the high-conductivity insert, and the optimized geometry and performance when the complexity (n_1) increases ($\tilde{k}=300$, $\phi_1=0.05$).

shows how the geometry optimized in this study responds when the number of elements n_1 increases. The external shape becomes less slender, and the peak temperature (minimized three times) decreases monotonically. The numerical values listed under each drawing show that the rate of decrease in $\tilde{T}_{\text{peak,min}}$ decreases

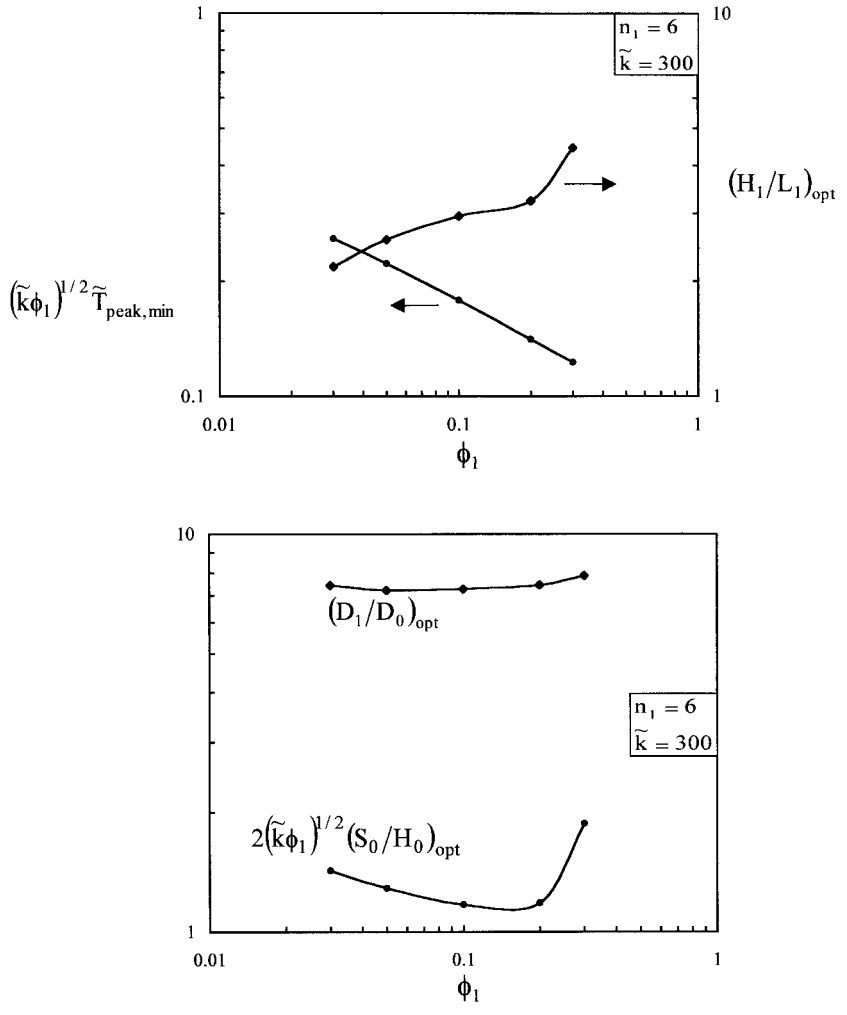

Fig. 5. The optimized first-assembly design as a function of the amount of high-conductivity material ($n_1 = 6$, $\tilde{k} = 300$).

as well, meaning that a point of diminishing returns is reached in this sequence of trading increased complexity in design for decreased overall resistance.

The relevant design question is how to select the external and internal dimensions of the configuration of Fig. 4 when the material parameters $\tilde{k}$ and ϕ_1 are specified. This information is provided in Figs. 5 and 6 for designs with $n_1 = 6$, because this is when the first-assembly structure is sufficiently complex to exhibit an overall resistance that is comparable with that of designs with larger n_1 values (see Fig. 7 later in this section).

Fig. 5 shows how the optimized design changes when the amount of high-conductivity material (ϕ_1) increases. The external shape $(H_1/L_1)_{opt}$ and the internal ratio $(D_1{:}D_0)_{opt}$ are relatively insensitive to ϕ_1 in the documented range $0.03 \leq \phi_1 \leq 0.3$, and perhaps even outside this range. The optimal tip spacing S_0 decreases as ϕ_1 increases: we plotted this result as the group $2(\tilde{k}\phi_1)^{1/2}(S_0/H_0)_{opt}$, where $H_0 = L_1/(n_1/2)$. The constancy of this group confirms once more the scaling argument that led to Eq. (9) and the rightmost columns of Tables 2 and 3. Finally, the minimized global resistance decreases as $\phi_1^{-1/2}$, which is why the group $(\tilde{k}\phi_1)^{1/2}\ \tilde{T}_{peak,min}$ plotted on the ordinate depends only weakly on ϕ_1. All these trends are emphasized by Fig. 6, which shows how the optimized design responds to changes in the conductivity ratio $\tilde{k}$.

6. First assembly with fixed external shape

Another design problem is the optimization of the conductive path of the first-assembly type in a space with constrained shape. This possibility was explored at the elemental level in a square domain (Table 3)

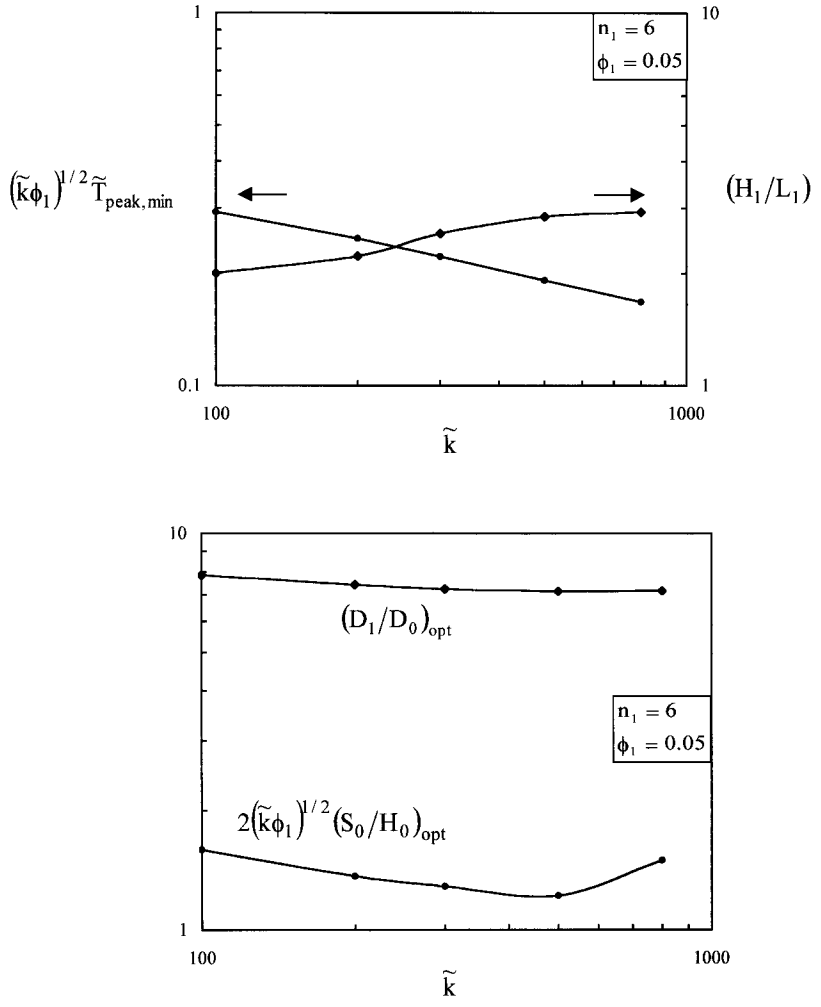

Fig. 6. The optimized first-assembly design as a function of the ratio of thermal conductivities ($n_1 = 6$, $\phi_1 = 0.05$).

and a round domain (Fig. 3). In Fig. 7 we show the optimized first-assembly geometry for a (k_0, k_p) composite material with $\tilde{k} = 300$ and $\phi_1 = 0.05$, which must fit in a square space. The upper images have been drawn to scale, and should be compared with the corresponding sequence shown in Fig. 4 (bottom) for the volume with unconstrained external shape. Note the similar tip spacings and k_p-blade thicknesses.

The minimized global resistance is indicated by $H_1/L_1 = 1$ in the lower part of Fig. 7. The lack of freedom in choosing the external shape is felt as an increase of the order of 20% in the global resistance. Fig. 7 also shows the point of diminishing returns that is reached when the internal complexity of the design increases: the optimized $n_1 = 6$ design is almost as good as the optimized $n_1 = 16$ design. This conclusion holds for both designs, constrained external shape ($H_1/L_1 = 1$) and unconstrained optimized shape, $(H_1/L_1)_{opt}$.

7. Optimal second-assembly geometry

The next step in the direction of increasing internal complexity is the second assembly shown in Fig. 8. The second assembly has the total size $A_2 = H_2L_2$, and contains n_2 first assemblies, $n_2 = A_2/A_1$. Fig. 8 was drawn for $n_2 = 2$. The heat currents collected by the first assemblies are channeled into a single new central blade of thickness D_2. The geometry of the second assembly depends on six dimensionless parameters: D_2/D_0, D_1/D_0, n_2, n_1, D_0/B_0 and H_2/L_2. The optimization was subjected to only two constraints, the total size A_2, and the fraction occupied by the high conductivity material, $\phi_2 = A_{p2}/A_2$. In other words, the optimization procedure is based on the largest number of degrees of freedom, as the optimized shapes determined at the elemental and first-assembly levels are not preserved at the second-assembly level. The design progresses

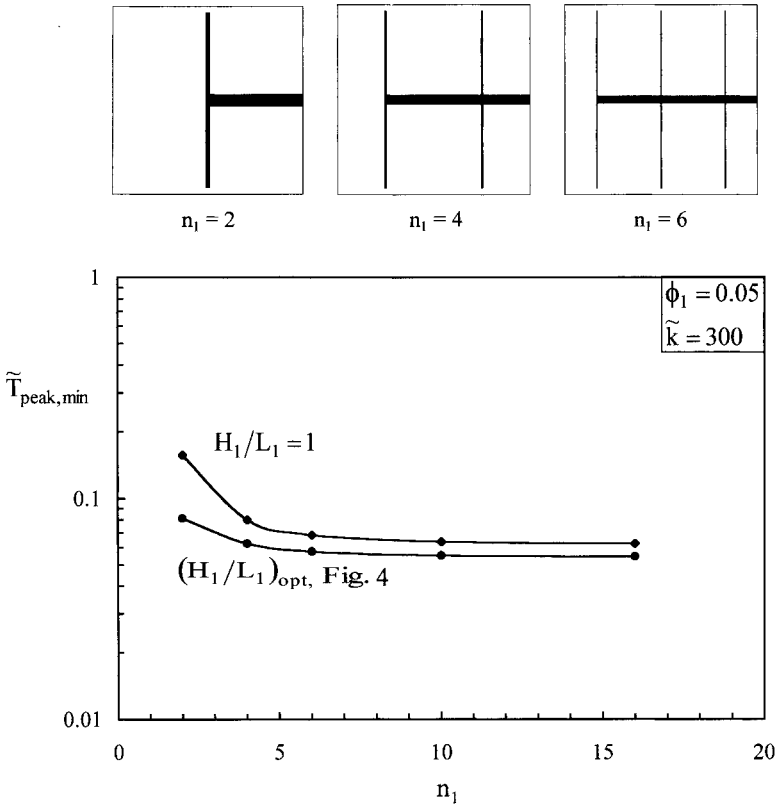

Fig. 7. The optimized first-assembly design when the external shape is constrained to a square ($\tilde{k}=300$, $\phi_1=0.05$).

inward, by increasing the complexity of the same system (the same overall size) that was optimized as an element or as a first assembly. For the numerical work we used the method of section 2, with ϕ_2, L_2 and A_2 in place of ϕ_0, L_0 and A_0 in Eqs. (2) and (3).

In the first phase of the numerical work we selected $\phi_2=0.1$ and $\tilde{k}=300$, and fixed three of the geometric parameters: $D_2/D_0=10$, $D_1/D_0=5$ and $n_2=2$. We minimized the peak dimensionless temperature, first, with respect to D_0/B_0, and then with respect to the external shape H_2/L_2. The results of this double optimization are presented in Fig. 9 as functions of the remaining parameter, n_1. The twice-minimized overall resistance of the second assembly ($\tilde{T}_{peak,mm}$) has a relatively shallow minimum with respect to n_1: the optimal number of elemental volumes in each first assembly is in the vicinity of $n_1=8$. The bottom part of Fig. 9 shows the corresponding tip spacings that characterize the optimized second assembly, and how they vary with n_1.

In the second phase of the optimization we fixed $n_1=8$, because the effect of n_1 on the optimized performance is weak, provided n_1 is of the same order of magnitude as the optimal value. We then repeated the procedure of Fig. 9 for many other combinations of D_2/D_0 and D_1/D_0. The results are summarized in Fig. 10, again, for $n_2=2$. Read from top to bottom, Fig. 10 shows the actual sequence in which we conducted the optimization. We first minimized $\tilde{T}_{peak}$ with respect to D_0/B_0, and produced the $\tilde{T}_{peak,m}$ function shown in the top frame of Fig. 10. This function was minimized next with respect to D_2/D_0 in the top frame, and with respect to D_1/D_0 in the middle frame. Finally, the twice-minimized overall resistance $\tilde{T}_{peak,mm}$ was minimized with respect to the external shape H_2/L_2 in the bottom frame. The results of this triple minimization are $\tilde{T}_{peak,mmm}=0.0353$, $(D_2/D_0)_{opt}=24.6$, $(D_1/D_0)_{opt}=8.03$ and $(H_2/L_2)_{opt}=1.784$. The optimized geometry and temperature field are presented to scale in Fig. 11 (left side).

Fig. 12 shows the other details of the geometry optimized in the sequence of Fig. 10. They show that the optimized design is sensitive to the final changes made in the selection of H_2/L_2. Fig. 12 is a continuation of the bottom frame of Fig. 10, which showed the sensitivity of the overall resistance to changes in H_2/L_2.

The remaining effect to document is that of the number of constituents in the second construct, n_2. We repeated the entire optimization sequence of Figs. 9–12

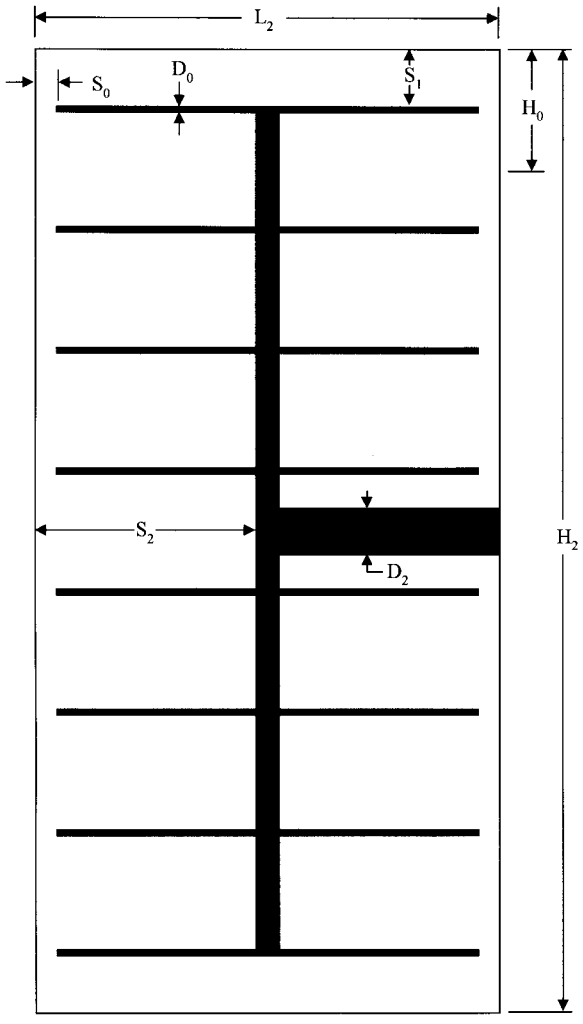

Fig. 8. Second-assembly configuration containing two first assemblies.

for $n_2=4$, and the resulting optimized architecture is shown on the right side of Fig. 11. At the end of the first phase of this optimization (in the equivalent of Fig. 9) we found that the optimal number of elemental systems in each first construct is $n_1=8$. We continued the optimization in the second phase by setting $n_1=8$, and executed the steps that correspond to the three frames of Fig. 10. The final, optimized geometry (Fig. 11, right side) is characterized by $\tilde{T}_{\text{peak,mmm}}=0.0319$, $(D_2/D_0)_{\text{opt}}=40.4$, $(D_1/D_0)_{\text{opt}}=9.79$ and $(H_2/L_2)_{\text{opt}}=1.724$. Noteworthy in the color display is the sharp temperature gradient in the thin space ($2\ S_0$) between the tips of two in-line elemental blades of thickness D_0. Although not very visible on the right side of Fig. 11, the tips of the elemental blades do not touch.

So far, the effect of increasing n_2 from 2 to 4 is to decrease the overall resistance $\tilde{T}_{\text{peak,mmm}}$ by 10%, while leaving the external shape $(H_2/L_2)_{\text{opt}}$ practically unchanged. Will these trends continue at even higher n_2 values? To answer this question we repeated the entire procedure of Figs. 9–12 for $n_2=6$ and $n_2=8$. The graphic details of this numerical work are omitted for brevity. The two main features of the optimized design are summarized in Fig. 13. Each design was optimized with respect to D_0/B_0, D_2/D_0, D_1/D_0 and H_2/L_2. We see that the overall resistance $\tilde{T}_{\text{peak,mmmm}}$ decreases gradually as n_2 increases, and that the rate of decrease slows down. The external aspect ratio $(H_2/L_2)_{\text{opt}}$ is almost insensitive to the increase in internal complexity. These trends agree qualitatively with what we learned from the inward optimization of the first assembly, specifically, Figs. 4 and 7. Most important is the absence of an optimal number of constituents (n_2) in the second assembly, which is contrary to the result found when the construction proceeds 'outward', i.e., where the optimized shape determined at the first-assembly level is retained at the second-assembly level [1].

The constancy of the external aspect ratio is important because it shows that some geometric features are robust: they are 'best' for many tree paths. More complex internal structures, however, will always be better than less complex structures. Performance increases (resistance decreases) as we move—in time—from the simplest internal structure (one blade, Fig. 1) to a more complex one (e.g., Fig. 8) in a system that has the same total volume. This is why nature 'makes' increasingly complex internal structures, even though the rate of improvement in performance decreases.

8. Conclusions

There are several basic aspects that have been brought to light in this study, and deserve to be emphasized. First the global performance of the optimized system improves as the internal complexity increases. To illustrate this trend, consider a system (A) with $\tilde{k}=300$ and $\phi=A_p/A=0.1$ optimized as an elemental system, first assembly, and second assembly. The results developed in this paper show that the global resistance of the optimized designs, $[(T_{\text{peak}}-T_{\text{sink}})/(q'''A/k_0)]_{\text{min}}$, decreases in this sequence: 0.0838, 0.0573 and 0.0304. Improvements are registered when the design becomes more complex, provided that all the geometric aspect ratios (internal and external) are optimized, and that the basic shape of the volume-to-point flow path is *the tree*.

These improvements become less and less dramatic as the complexity increases. From an engineering standpoint this means that there comes a point where

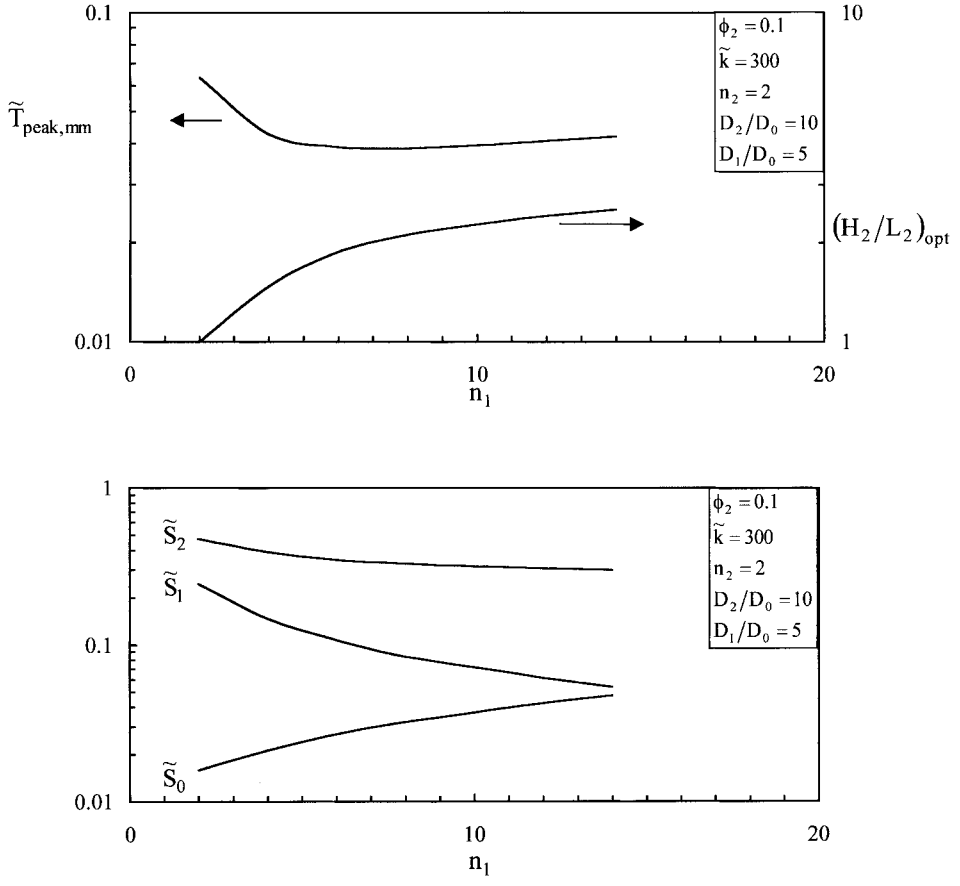

Fig. 9. The optimization of the second assembly with respect to the first three degrees of freedom, D_0/B_0, H_2/L_2 and n_1.

further increases in complexity are not justified by the increases in the costs associated with executing (e.g., manufacturing) the device. This is why summaries such as Figs. 7 and 13 are important, and why the optimal numbers of constituents produced by the 'outward' approach [1] can be used as rough estimates of the numbers of constituents (n_1, n_2, ...) that may prove to be adequate. For example, for a first-assembly structure with $\tilde{k}=300$ and $\phi_1=0.1$, the results of Ref. [1] recommend $n_{1,opt}=4$, which is comparable with the n_1 value where the substantial drop in $\tilde{T}_{peak,min}$ has already been achieved.

Another important aspect is that every time we give the design more degrees of freedom, and we optimize it in these additional directions, the global performance of the optimized structure improves. In this paper we explored two new ways of introducing degrees of freedom in the optimization. One was the decision that in each new assembly the shapes of the previous (smaller) assemblies are free to be optimized once more. The other was the decision to provide spacings (k_0 material) beyond the tips of all the high-conductivity blades, and to optimize these spacings. Further improvements can be sought by optimizing the angle between each central k_p blade and its tributaries, and by optimizing the manner in which the thickness of each k_p blade varies with longitudinal position: these directions have been explored in Ref. [9], which showed that the relative improvements in global performance are of the order of 5%, i.e., less than the improvements brought by the tip spacings optimized in this paper (see the discussion under eq. (8)).

Finally, when the structure is complex (e.g., second assembly) and already has the shape of a tree with geometric aspect ratios close to the optimal values, the minima with respect to the various degrees of freedom are relatively shallow. This means that a multitude of designs that do not look exactly like the optimal structure perform essentially at the same high level as the optimal structure. The conclusion is that the near-opti-

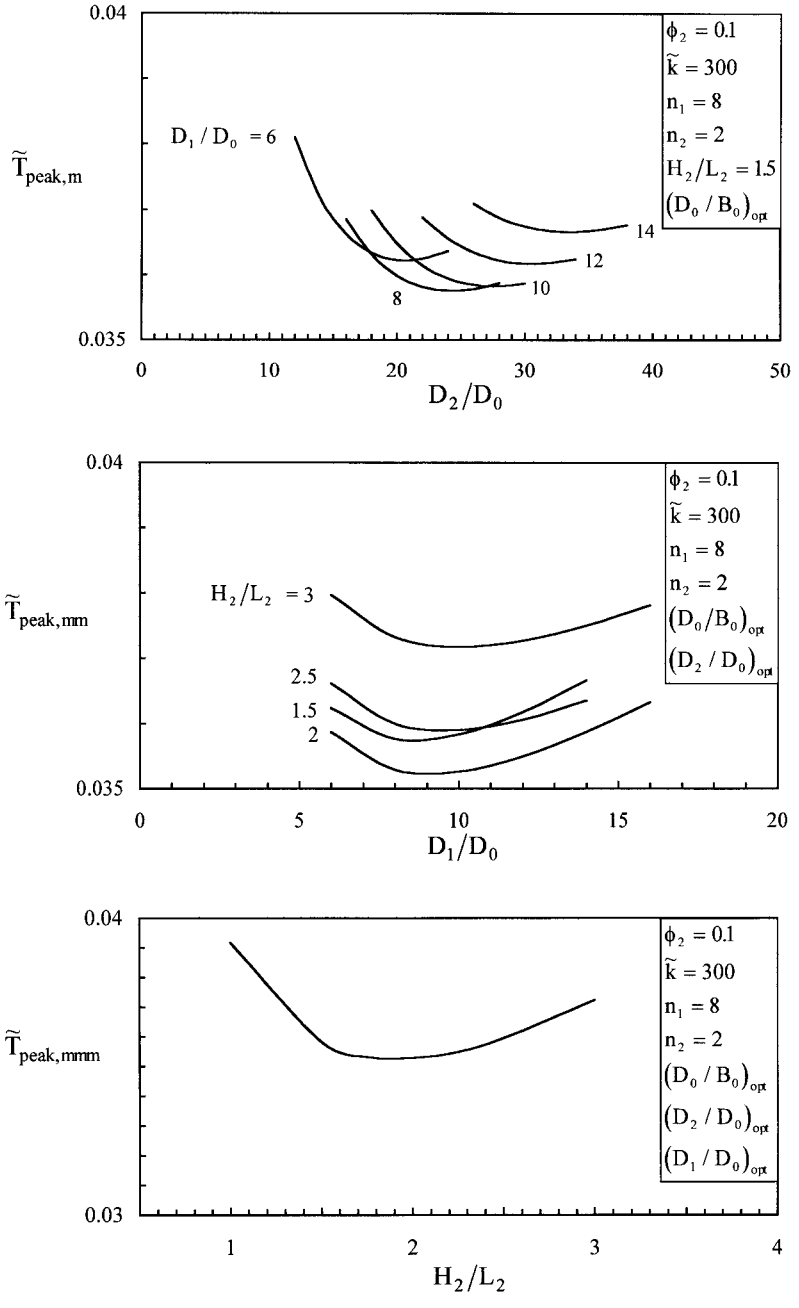

Fig. 10. The optimization of the second assembly with respect to the four geometric aspect ratios D_0:B_0, D_2:D_0, D_1:D_0, H_2:L_2).

mal tree structures represent a *robust* design: minor changes in internal and external shapes have almost no effect on the global performance of the design. We also found that certain optimized geometrical features are relatively invariant from one design to the next. Note, for example, the external aspect ratio of the second-assembly structure (Fig. 13). Such invariants may be relied upon when seeking to simplify the numerical work by reducing the degrees of freedom in the optimization procedure.

The readers interested in the applications of constructal theory to predicting the geometry of natural flow systems are directed to the 1997 review [7], and to more recent extensions: Bénard convection in clear

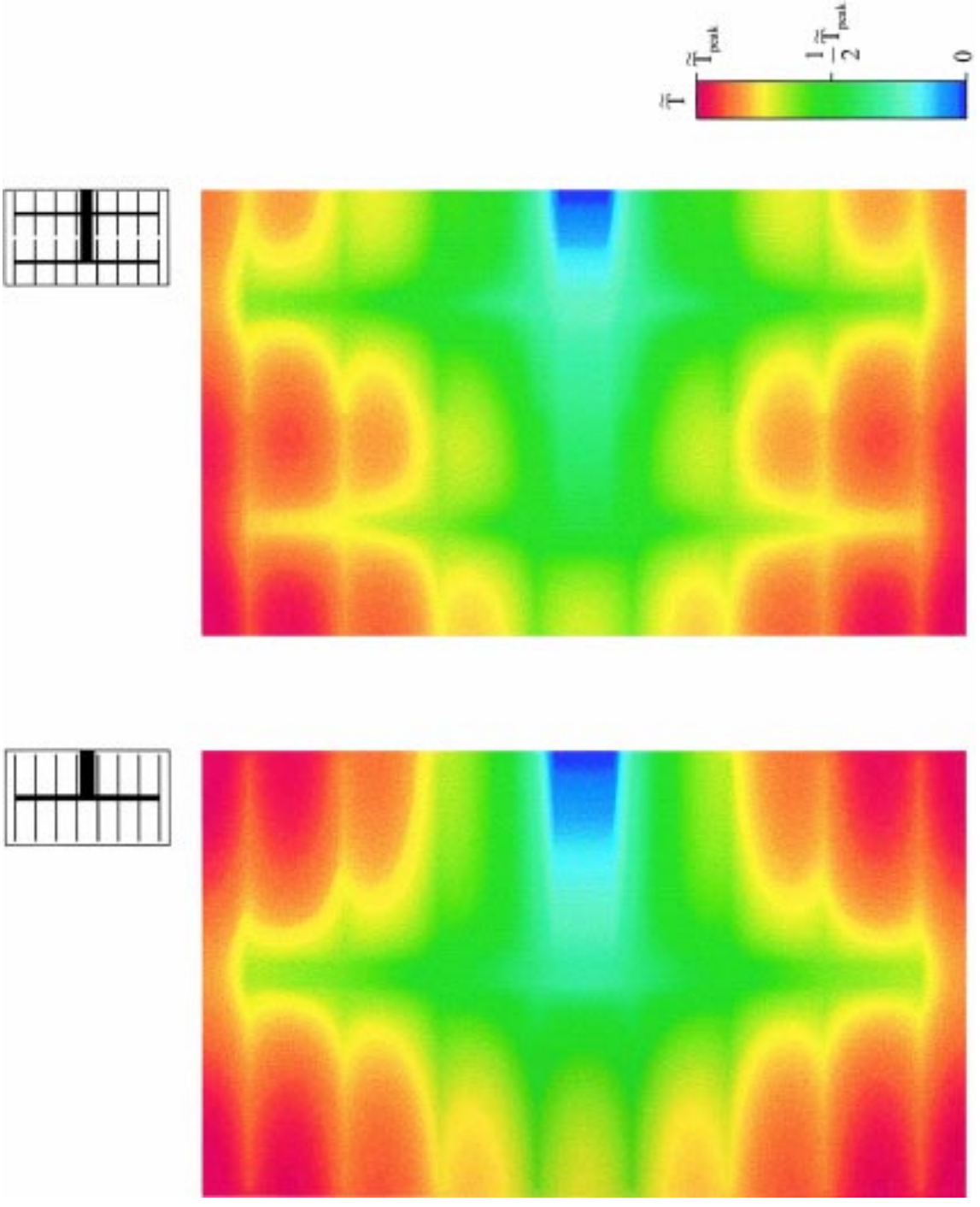

Fig. 11. The internal and external geometry of the optimized second construct with $\phi_2 = 0.1$, $\tilde{k} = 300$ and $n_1 = 8$. Left side: $n_2 = 2$. Right side: $n_2 = 4$.

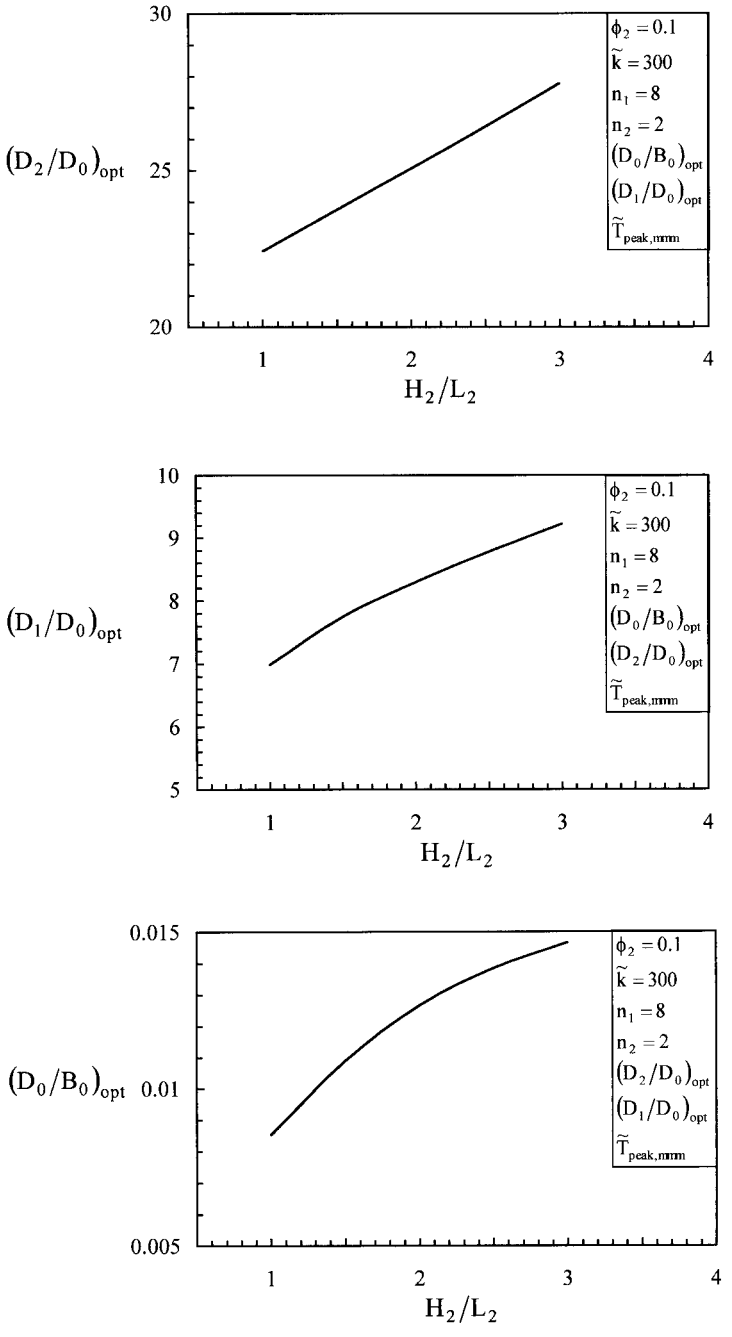

Fig. 12. The sensitivity of the optimized second construct (Fig. 10) to changes in the external shape H_2/L_2.

fluids and fluid-saturated porous media [10], lightning, or the time-dependent discharge of a volume to one point sink [11], patterns of cracks in volumetrically shrinking solids [12], river drainage basins [13], three-dimensional trees [14], and street patterns and urban growth [15].

Acknowledgements

This work was supported by the National Science Foundation and the General Organization for Technical Education and Vocational Training, Riyadh, Saudi Arabia. The authors thank Prof. Dusan P.

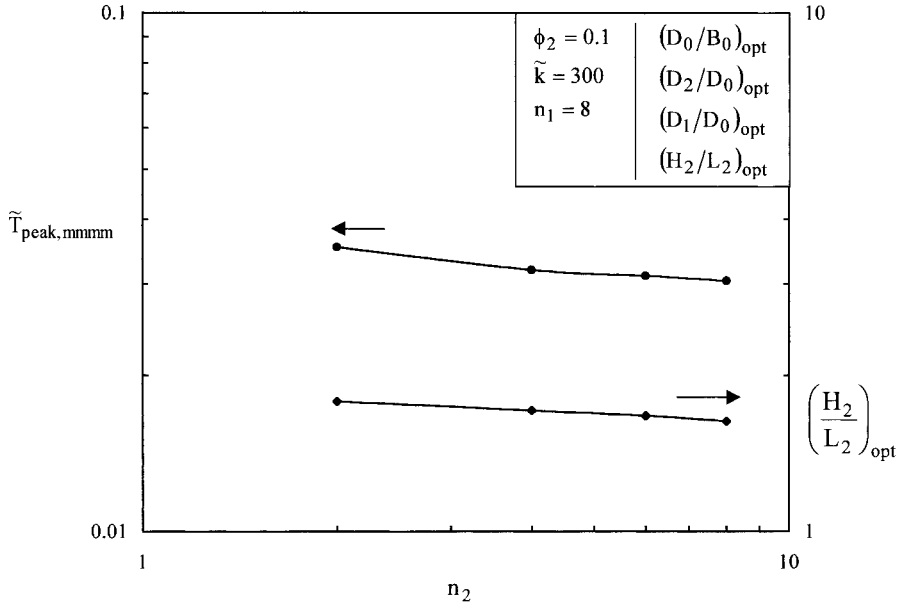

Fig. 13. The optimized external shape and performance of the second-assembly configuration when the complexity (n_2) increases.

Sekulic, University of Kentucky, for the many constructive comments made on the original manuscript.

References

[1] A. Bejan, Constructal-theory network of conducting paths for cooling a heat generating volume, International Journal of Heat and Mass Transfer 40 (1997) 799–816.

[2] G.P. Peterson, A. Ortega, Thermal control of electronic equipment and devices, Advances in Heat Transfer 20 (1990) 181–314.

[3] R.W. Knight, J.S. Goodling, D.J. Hall, Optimal thermal design of forced convection heat sinks-analytical, Journal of Electronic Packaging 113 (1991) 313–321.

[4] N.K. Anand, S.H. Kim, L.S. Fletcher, The effect of plate spacing on free convection between heated parallel plates, Journal of Heat Transfer 114 (1992) 525–528.

[5] S.H. Kim, N.K. Anand, Laminar developing flow and heat transfer between a series of parallel plates with surface mounted discrete heat sources, International Journal of Heat and Mass Transfer 37 (1994) 2231–2244.

[6] W. Li, S. Kakac, F.F. Hatay, R. Oskay, Experimental study of unsteady forced convection in a duct with and without arrays of block-like electronic components, Wärme und Stoffübertragung 28 (1993) 69–79.

[7] A. Bejan, Advanced Engineering Thermodynamics, Wiley, New York, 1997.

[8] FIDAP Theory Manual 70, Fluid Dynamics International, Evanston, IL, 1993.

[9] G.A. Ledezma, A. Bejan, M.R. Errera, Constructal tree networks for heat transfer, Journal of Applied Physics 82 (1997) 89–100.

[10] R.A. Nelson Jr, A. Bejan, Constructal optimization of internal flow geometry in convection, Journal of Heat Transfer 120 (1998) 357–364.

[11] N. Dan, A. Bejan, Constructal tree networks for the time-dependent discharge of a finite-size volume to one point, Journal of Applied Physics 84 (6) (1998) 3042–3050.

[12] A. Bejan, Y. Ikegami, G.A. Ledezma, Constructal theory of natural crack pattern formation for fastest cooling, International Journal of Heat and Mass Transfer 41 (1998) 1945–1954.

[13] M.R. Errera, A. Bejan, Deterministic tree networks for river drainage basins, Fractals 6 (3) (1998) 245–261.

[14] G.A. Ledezma, A. Bejan, Constructal three-dimensional trees for conduction between a volume and one point, Journal of Heat Transfer 120 (1998) 977–984.

[15] A. Bejan, G.A. Ledezma, Streets tree networks and urban growth: optimal geometry for quickest access between a finite-size volume and one point, Physica A 225 (1998) 211–217.